Nanoscale Advances

ROYAL SOCIETY OF CHEMISTRY

PAPER

Published on 28 April 2026

Cite this: DOI: 10.1039/d6na00118a

Investigation of the chemical structure of core–shell Fe_3O_4@$Ni_{1-x}Co_xFe_2O_4$ nanoparticles and its influence on their magnetic properties

Raul Lopez-Martin, †[a] Iryna Makarchuk,†[b] Fadi Choueikani,[c] Simon Hettler,[def] Raul Arenal,[efg] Jose A. De Toro[a] and Benoit P. Pichon *[bh]

Core–shell ferrite nanoparticles offer a promising route toward high-performance, rare-earth-free magnetic nanomaterials, yet fine control over interfacial exchange coupling remains a critical challenge. Here, we report the synthesis of Fe_3O_4@$Ni_{1-x}Co_xFe_2O_4$ nanoparticles *via* a two-step seed-mediated thermal decomposition process in organic media, enabling systematic tuning of the shell composition and size of the pristine Fe_3O_4 nanoparticles. High-resolution scanning transmission electron microscopy (STEM) and electron energy loss spectroscopy (EELS) analyses confirm the formation of an epitaxial spinel shell, with excellent crystallographic continuity and homogeneous spatial cation distribution. X-ray absorption spectroscopy (XAS) and X-ray magnetic circular dichroism (XMCD) reveal that Co^{2+} and Ni^{2+} cations preferentially occupy octahedral sites while a minor -but significant-$Ni_{1-x}Co_xO$ wüstite phase forms at the periphery, as also suggested by microscopy, introducing small exchange-bias effects. Alongside the exchange bias effect, a comprehensive magnetic characterization using SQUID magnetometry revealed the role of both the shell composition and the surface anisotropy, the latter being dominant over the shell composition when the core nanoparticle size was reduced. This multi-technique study unveils the formation mechanism of such core–shell bimagnetic nanoparticles and the intricate interplay between composition, interface structure, and magnetic behavior. It provides a potential framework for designing chemically engineered, anisotropy-tailored magnetic nanostructures for spintronic, biomedical, and high-density data storage applications.

Received 13th February 2026
Accepted 12th March 2026

DOI: 10.1039/d6na00118a

rsc.li/nanoscale-advances

Introduction

Magnetic nanoparticles (MNPs) have garnered immense interest due to their unique size-dependent properties stemming from finite-size and surface effects, positioning them as versatile candidates for applications ranging from magnetic resonance imaging and targeted drug delivery to magnetic hyperthermia and photomagnetic devices.[1] Their superparamagnetic behavior at ambient temperature—a direct consequence of reduced dimensions—emerges when thermal energy exceeds the magnetic anisotropy energy, enabling spontaneous fluctuations of the magnetic moment around the easy axis of magnetization.[2]

Within this framework, the design of complex nanostructures has unlocked new avenues for engineering and optimizing magnetic behavior.[3] Over the past two decades, significant efforts have been devoted to extending the superparamagnetic limit beyond room temperature—a prerequisite for advanced technologies such as high-density magnetic storage and permanent magnets—while preserving the desirable features imparted by nanoscale confinement. A particularly elegant and effective approach involves enhancing the magnetic anisotropy through interfacial exchange coupling between magnetically soft and hard phases.[4] In such systems, the rotation of the soft spins is hindered by the uncompensated hard spins -with a preferential direction set by field cooling below the ordering temperature of the hard magnetic phase-at the interface, thereby amplifying the overall anisotropy without necessitating large quantities of rare or costly elements.[5,6]

[a]Instituto Regional de Investigación Científica Aplicada (IRICA) and Departamento de Física Aplicada, Universidad de Castilla-La Mancha, 13071, Ciudad Real, Spain
[b]Université de Strasbourg, CNRS, Institut de Physique et Chimie des Matériaux de Strasbourg, UMR 7504, F-67000 Strasbourg, France. E-mail: benoit.pichon@ipcms.unistra.fr
[c]Synchrotron SOLEIL, L'Orme des Merisiers, Departementale 128, 91190 Saint-Aubin, France
[d]Laboratoty for Electron Microscopy (LEM), Karlsruhe Institute for Technology, Engesserstr. 7, 76131 Karlsruhe, Germany
[e]Instituto de Nanociencia y Materiales de Aragon (INMA), CSIC-Universidad de Zaragoza, Calle Pedro Cerbuna 12, 50009 Zaragoza, Spain
[f]Laboratorio de Microscopías Avanzadas (LMA), Universidad de Zaragoza, Calle Mariano Esquillor, 50018 Zaragoza, Spain
[g]ARAID Foundation, 50018 Zaragoza, Spain
[h]Institut Universitaire de France, 75231 CEDEX 05 Paris, France
† These authors have contributed equally to this work.

When achieved in a core–shell geometry, this strategy allows for a synergistic interplay between phases *via* crystallographic interfaces, wherein rigid exchange coupling can result in smooth hysteresis loops—distinct from the stepped behavior observed in spring magnets—thereby enabling tunable and coherent magnetic responses. The degree of exchange coupling is highly sensitive to the relative magnetic anisotropy of the core and shell, which depend of several parameters, notably their volume ratio, interface quality, and chemical composition.[7–14]

Ferrites (MFe_2O_4, where M is a divalent transition metal ion) represent an ideal materials platform for constructing such bimagnetic nanostructures due to their wide range of chemical compositions and associated magnetic properties.[15] The ability to tune cation distribution between tetrahedral (T_d) and octahedral (O_h) sites in the spinel lattice provides a powerful handle for engineering magnetic behavior.[16–19] Moreover, the structural similarity across ferrites, including closely matched lattice parameters, facilitates high-quality crystallographic interfaces. For instance, combining two ferrites with contrasting anisotropies (K being the magnetic anisotropy constant), $NiFe_2O_4$ ($K \approx 1$ kJ m^{-3}) and $CoFe_2O_4$ ($K \approx 290$ kJ m^{-3}) has been shown to substantially enhance the effective magnetic anisotropy in core–shell geometries.[20–22]

Achieving such structural and magnetic precision relies critically on the synthesis methodology. The thermal decomposition of organometallic precursors at elevated temperatures (~310 °C) in high-boiling-point solvents has emerged as a robust route for producing monodisperse nanoparticles with narrow size distributions and controlled morphologies.[23–26] When implemented in a multistep, seed-mediated growth process, this technique enables the construction of tailored nanostructures with well-defined structure.[6,8,9,13,27–30] More recently, this approach has evolved to include multi-shell, also called "onion-like", architectures through iterative shell deposition, offering further opportunities for modulating magnetic interactions.[31–36]

The achievement and understanding of such advanced heterostructures have been greatly facilitated by state-of-the-art characterization tools. Scanning transmission electron microscopy (STEM) combined with electron energy loss spectroscopy (EELS) provides nanoscale insights into local elemental distribution and oxidation states.[37] X-ray absorption spectroscopy (XAS) and its magnetic variant, X-ray magnetic circular dichroism (XMCD), enable the elucidation of cationic valence and site occupancy in complex spinel matrices—capabilities essential when traditional techniques such as X-ray diffraction fall short in resolving structurally similar phases like Fe_3O_4 and $CoFe_2O_4$.[38] These advanced tools have revealed that core–shell nanoparticles often deviate from idealized models: interfacial cation diffusion and partial solubilization/recrystallization result in graded compositions across the interface rather than abrupt phase boundaries.[35,39–42]

In the present work, we report the synthesis of bimagnetic core–shell nanoparticles composed of a Fe_3O_4 core and a $Ni_{1-x}Co_xFe_2O_4$ shell, in which the shell composition is systematically varied to probe its influence on their magnetic properties. The nanoparticles were synthesized *via* a seed-mediated growth protocol based on sequential thermal decomposition of metal precursors in organic media. Comprehensive characterization was carried out using a combination of conventional techniques (TEM, Fourier transform infrared (FTIR) spectroscopy, thermal gravimetry (TG) analysis) alongside advanced structural and spectroscopic tools (STEM-EELS, HRTEM, XAS, XMCD). This multipronged approach enabled an unprecedented level of insight into the spatial distribution of metal cations, crystallographic integrity, and oxidation states—revealing a nuanced chemical landscape within the core–shell framework. These detailed structural and chemical insights provide a robust basis for correlating compositional gradients and interface quality with the resulting magnetic behavior, thus paving the way for the design of next-generation magnetic nanomaterials with tailored anisotropy and performance.

Experimental section

Synthesis of bimagnetic core–shell nanoparticles

Most of the metal precursors used for nanoparticle synthesis were synthesized. Protocols and characterization are detailed in SI.[43,44]

Caution. The synthesis of nanoparticles being performed without magnetic stirring, careful awareness and assessment of potential safety risks are essential to prevent hazards such as overheating or fire, particularly when working with high-boiling, flammable solvents (dioctyl ether) and elevated temperatures (290 °C).

The pristine iron oxide nanoparticles (P1) used for the synthesis of FeCo, FeNi and FeCoNi_10 were synthesized following an already published protocol.[25] A two-necked round-bottom flask was filled with 1.38 g (2.22 mmol) of iron(II) stearate, 1.254 g (4.44 mmol) of oleic acid (99% Alfa Aesar) and 20 mL of ether dioctyl (BP = 290 °C, 97% Fluka). The brownish mixture was heated at 120 °C under a magnetic stir for 30 min in order to remove water residues and to homogenize the solution. The magnetic stirrer was then removed and the flask was connected to a reflux condenser before heating the solution to reflux for 2 h with a heating ramp of 5 °C min^{-1}. At the end, the mixture was allowed to cool to 100 °C. A portion of the solution (4 mL for FeCo, 10 mL for FeNi and FeCoNi_10) was kept as a reference of the core nanoparticles to analyze following an already published protocol.[45] After cooling down to room temperature, the NPs were precipitated by the addition of acetone and then washed by centrifugation in a mix of chloroform and acetone. They were then stored in 20 mL of chloroform.

FeCo nanoparticles. 0.141 g (0.22 mmol) of cobalt(II) stearate, 1.254 g (4.44 mmol) of oleic acid (99% Alfa Aesar) and 20 mL of 1-octadecene (BP = 315 °C, 95% Sigma-Aldrich) were added to the solution of pristine iron oxide nanoparticles P1 (16 mL). The mixture was heated to 120 °C for 30 min under magnetic stirring to remove water residues and to homogenize the solution. After removal of the magnetic stirrer, the flask was then connected to a reflux condenser to heat the solution at reflux for another 3 h with a heating ramp of 1 °C min^{-1}. After cooling to room temperature, the nanoparticles were precipitated by the addition of acetone and then washed by centrifugation in a mix

of chloroform and acetone. They were then stored in chloroform.

FeNi nanoparticles. 0.074 g (0.22 mmol) of nickel(II) octanoate, 1.254 g (4.44 mmol) of oleic acid, and 20 mL of 1-octadecene were added to the solution of pristine iron oxide nanoparticles P1 (16 mL). The mixture was heated to 120 °C for 30 min under magnetic stirring to remove water residues and to homogenize the solution. After removal of the magnetic stirrer, the flask was then connected to a reflux condenser to heat the solution at reflux one hour with a heating ramp of 1 °C min^{-1}. After cooling to room temperature, the nanoparticles were precipitated by the addition of acetone and then washed by centrifugation in a mix of chloroform and acetone. They were then stored in chloroform.

FeCoNi_10 nanoparticles. 0.135 g (0.22 mmol) of the mixed stearate precursor $Co_{0.5}Ni_{0.5}St_2$, 1.254 g (4.44 mmol) of oleic acid (99% Alfa Aesar) and 20 mL of 1-octadecene were added to the solution of pristine iron oxide nanoparticles P1 (16 mL). The mixture was heated to 120 °C for 30 min under magnetic stirring to remove water residues and to homogenize the solution. After removal of the magnetic stirrer, the flask was then connected to a reflux condenser to heat the solution at reflux for 2 h with a heating ramp of 5 °C min^{-1}. After cooling to room temperature, the nanoparticles were precipitated by the addition of acetone and then washed by centrifugation in a mix of chloroform and acetone. They were then stored in chloroform.

The synthesis of FeCoNi_14 nanoparticles was performed from larger pristine iron oxide nanoparticles (P2)·In contrast to P1, the protocol requires commercial iron(III) stearate details are given in our previous reports.[27,31] A two-necked round-bottom flask was filled with 2 g (2.2 mmol) of commercial iron(III) stearate, 1.24 g (4.4 mmol) of oleic acid (99% Alfa Aesar), 20 mL of ether dioctyl (BP = 290 °C, 97% Fluka). The brownish mixture was heated at 120 °C under a magnetic stir for 1 hour in order to remove water residues and to homogenize the solution. The magnetic stirrer was then removed and the flask was connected to a reflux condenser before heating the solution to reflux for 2 h with a heating ramp of 5 °C min^{-1}. At the end, the mixture was allowed to cool to 100 °C. After cooling down to room temperature, the NPs were precipitated by the addition of acetone and then washed by centrifugation in a mix of chloroform and acetone. They were then stored in 20 mL of chloroform.

FeCoNi_14 nanoparticles. 0.27 g (0.44 mmol) of the mixed stearate precursor $Co_{0.5}Ni_{0.5}St_2$ and 20 mL of 1-octadecene were added to the solution of large pristine iron oxide nanoparticles P1 (16 mL). The mixture was heated to 120 °C for 30 min under magnetic stirring to remove water residues and to homogenize the solution. After removal of the magnetic stirrer, the flask was then connected to a reflux condenser to heat the solution at reflux for 2 h with a heating ramp of 5 °C min^{-1}. After cooling to room temperature, the nanoparticles were precipitated by the addition of acetone and then washed by centrifugation in a mix of chloroform and acetone. They were then stored in chloroform.

Characterization techniques

Transmission electron microscopy. The TEM images for the size distribution analysis were taken on JEOL 2100 LaB6 microscope with a 0.2 nm point-to-point resolution. The high-resolution TEM and energy dispersive spectroscopy EDS were used to confirm the crystal structure and Fe and Co atomic distribution within synthesized nanoparticles, respectively.

Scanning transmission electron microscopy (STEM) and electron energy-loss spectroscopy (EELS). STEM imaging and STEM-EELS were performed in a probe-corrected Titan Low-Base (Thermo Fisher Scientific) equipped with a high-brightness field emission gun. The gun was operated at 300 keV for STEM imaging with a high-angle annular dark field (HAADF) detector with an acceptance angle of 48 mrad. STEM-EELS data was acquired at 80 keV with a Gatan Image Filter (GIF) Tridiem 866 with an acceptance angle of 87 mrad. Convergence angle for both imaging and spectroscopy was 25 mrad. The EELS spectrum imaging (SI) data was acquired with a dispersion of 0.3 eV to encompass the ionization edges of oxygen K, iron L, cobalt L and nickel L. Data analysis was conducted using a custom Matlab program. For elemental quantification, the pre-edge EEL spectra were first fitted by a power-law function. The background-spectra were then integrated in an energy window with a width of 30 eV. Relative atomic concentrations were obtained using calculated theoretical cross sections.[46] The overlap of the nickel $L_{3,2}$ edge with the iron L_1 edge was corrected using the iron $L_{3,2}$ edge intensity and an experimentally determined intensity ratio between iron $L_{3,2}$ and L_1 edges as described recently.[1] Line spectra profiles across the NPs were obtained by averaging several pixels to improve the signal-to-noise ratio. For the STEM analyses, the NPs were dispersed in ethyl alcohol and drop-casted on holey-carbon TEM grids followed by a ligand-cleaning process based on activated carbon. This cleaning process improves image quality and reduces beam damage. EELS-SI data was acquired on various individual NPs from each specimen, the data presented in the manuscript represents exemplary data.

Inductively coupled plasma-atomic emission spectrometry (ICP-AES). Measurements were performed by the Plateforme Analytique of the Institut Pluridisciplinaire Hubert Curien (UMR CNRS 7178), Strasbourg, France. Samples were mineralized at 185 °C for 50 min under pressure (Multiwave ECO, Anton Paar) with HCl (3 mL) for Fe, Co and Ni loading determination. Blank tests were carried out in parallel under the same conditions. Quantifications of metals in the clear obtained solutions were carried out by ICP-AES (Varian 720 ES) at two wavelengths: 250.690 nm and 251.611 nm.

X-ray diffraction. The XRD patterns of the synthesized nanoparticles were recorded at a Bruker D8 Advance diffractometer equipped with a non-monochromatic copper radiation (Kα = 0.154056 nm) and a Sol-X detector in the range from 20 to 80° 2θ with a step of 0.02°. High-purity silicon powder (a = 0.543082 nm) was systematically used as an internal standard. Refinement of XRD patterns were performed by using Fullprof software.

Fourier transform infra-red (FT-IR) spectroscopy was performed using a PerkinElmer Spectrum spectrometer in the energy range 4000–400 cm^{-1} on samples diluted in KBr pellets.

Themogravimetry analyses (TGA) were performed using a SDTQ600 from TA instrument. Measurements were performed on dried powders under air in the temperature range of 20 to 600 °C at a heating rate of 5 °C min^{-1}.

X-ray spectroscopy (XAS) and X-ray magnetic circular dichroism (XMCD). Spectra were recorded at the $L_{2,3}$ edges of Fe and Co, on the DEIMOS beamline at SOLEIL (Saclay, France).[47] All spectra were recorded at 4.2 K under UHV conditions (10^{-10} mbar) and using total electron yield (TEY) recording mode. The measurement protocol was previously detailed by Daffé et *al.*[48] An external parallel magnetic field H^+ (respectively antiparallel H^-) was applied on the sample while a σ_+ polarized (σ_- polarized respectively) perpendicular beam was directed on the sample. Isotropic XAS signals were obtained by taking the mean of the $\sigma_+ + \sigma_-$ sum where $\sigma_+ = [\sigma_L(H^+) + \sigma_R(H^-)]/2$ and $\sigma_- = [\sigma_L(H^-) + \sigma_R(H^+)]/2$ with σ_L and σ_R the absorption cross section measured respectively with left and right circularly polarized X-rays. XMCD spectra were obtained by taking the $\sigma_+ - \sigma_-$ dichroic signal with a ± 6.5 T applied magnetic field. The circularly polarized X-rays are provided by an Apple-II HU-52 undulator for both XAS and XMCD measurements while EMPHU65 with a polarization switching rate of 10 Hz was used to record hysteresis cycle at fixed energy.[49] Measurements were performed between 700 and 740 eV at the iron edge and between 770 and 800 eV at the cobalt edge with a resolution of 100 meV and a beam size of 800*800 μm. Both XMCD and isotropic XAS signals presented here are normalized by dividing the raw signal by the edge jump of the isotropic XAS. The samples consist of drop casted suspension of nanoparticles in chloroform onto a silicon substrate. The substrates were then affixed on a sample holder.

Superconducting quantum interference device (SQUID) magnetometry. Magnetic measurements were performed in using a SQUID magnetometer from Quantum Design MPMS-XL. Temperature dependent zero-field cooled (ZFC) and field cooled (FC) magnetization curves were recorded as follows: the sample was introduced in the SQUID at room temperature and cooled down to 5 K with no applied magnetic field and after applying a careful degaussing procedure. Then, a magnetic field of 75 Oe (7.5 mT) was applied, and the ZFC magnetization curve was recorded upon heating from 5 to 400 K. The sample was then cooled down to 5 K under the same applied field, and the FC magnetization curve was recorded upon heating from 5 to 400 K. Magnetization curves as a function of a magnetic field (M(H) curves) were measured at 5 and 300 K. The sample was also introduced in the SQUID at high temperature and cooled down to 5 K with no applied magnetic field (ZFC curve) and after applying a subsequent degaussing procedure. The magnetization was then measured at constant temperature by sweeping the magnetic field from +50 kOe to −50 kOe, and then from −50 kOe to +50 kOe. To evidence exchange bias effect, FC M(H) curves were further recorded after heating up at 400 K and cooling down to 5 K under a magnetic field of 50 kOe. The FC hysteresis loop was then measured by applying the same field sweep as for the ZFC hysteresis loop. The coercive field (H_C) and the M_R/M_S ratio were measured from ZFC and FC M(H) curves. The exchange bias field (H_E) was measured from FC M(H) curves. Saturation magnetization (M_S) was measured from the hysteresis loops recorded at 5 K.

Results and discussion

The synthesis strategy of bimagnetic core–shell nanoparticles consists in a two-step-seed-mediated growth (Fig. 1). First, pristine iron oxide ($Fe_{3-\delta}O_4$) nanoparticles (P1) were synthesized by controlling the thermal decomposition of iron(II) stearate ($FeSt_2$) at reflux of 1-octadecene (bp: 315 °C), a high-temperature boiling solvent. Nanoparticles were washed before the growth of the shell in order to avoid any unreacted and intermediate products. These nanoparticles correspond to Fe_3O_4 with partial oxidation at their surface.[9,25] Second, $Ni_{1-x}Co_xFe_2O_4$ was grown as a shell at the surface of iron oxide nanoparticles which act as crystal seeds upon the thermal decomposition of the corresponding metal complexes (see supporting information). Cobalt stearate ($CoSt_2$), nickel octanoate ($NiOct_2$) or mixed cobalt/nickel stearate ($Co_{0.5}Ni_{0.5}St_2$) were decomposed to release Fe_3O_4@$CoFe_2O_4$, Fe_3O_4@$NiFe_2O_4$ and Fe_3O_4@$Co_{1-x}Ni_xFe_2O_4$ core–shell nanoparticles, named FeCo, FeNi, FeCoNi_10, respectively. In addition, Fe_3O_4@$Co_{1-x}Ni_xFe_2O_4$ nanoparticles were also synthesized from iron oxide nanoparticles (P2) with a larger size of 14 ±

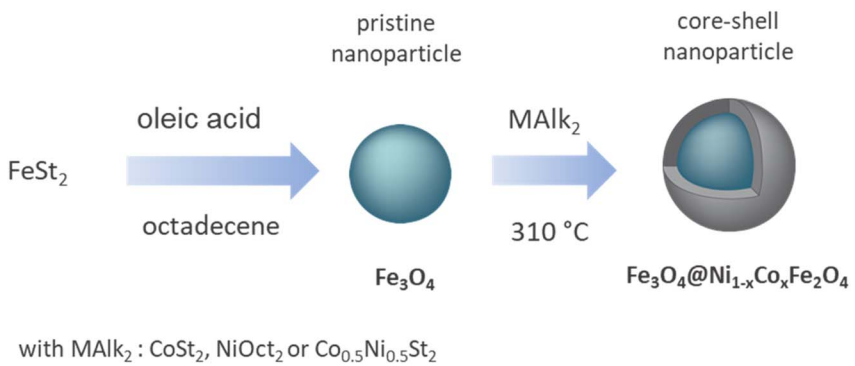

Fig. 1 Schematic illustration of the pathway for the synthesis of core–shell Fe_3O_4@$Ni_{1-x}Co_xFe_2O_4$ nanoparticles.

1.1 nm (Fig. S4). This sample was named FeCoNi_14. Each metal complex was characterized by FTIR spectroscopy (Fig. S1) and TG analysis (Fig. S2) in order to be selected to decompose near the boiling temperature of 1-octadecene. No iron stearate was added, the formation of the MFe_2O_4 shell happens through the partial solubilization of pristine iron oxide nanoparticles. As we recently reported on similar core–shell nanoparticles,[35] iron species are released before undergoing co-crystallization with the readily decomposed Co and/or Ni species. Both steps were performed in the presence of oleic acid which participates in the kinetic of the reaction[43] and allows the delivery of nanoparticles coated by oleic acid as shown by infrared spectroscopy (Fig. S6 and S7). Therefore, nanoparticles are not in direct contact as shown by TEM micrographs. Thanks to such a stabilizing agent, highly stable colloidal suspensions of non-aggregated nanoparticles can be prepared in organic solvents.

According to TEM micrographs (Fig. S3), iron oxide nanoparticles synthesized for each sample display a narrow size distribution and a well-defined shape, close to spheres although some sharp edges relate to faceted nanoparticles. After the second synthesis step, narrow size distribution is also observed although facets become larger (Fig. 2). The mean size of all nanoparticles increases, testifying to the formation of an extra layer at their surface due to the epitaxial growth of MFe_2O_4 shell from the surface of the Fe_3O_4 core. The apparent shell thickness was calculated to be half of the difference between the mean size of core–shell Fe_3O_4@$Ni_{1-x}Co_xFe_2O_4$ and pristine Fe_3O_4 nanoparticles. Similar conclusions can be drawn for FeCoNi_12 and FeCoNi_14 (Fig. S4 and S5). It is worth noting that the mean thickness is around 0.5 nm (half of size variation). This value is smaller than the cell parameter of the corresponding ferrites (around 8.33 to 8.39 Å) which, in principle, are expected to be formed.

Scanning transmission electron microscopy – high-angle annular dark-field (STEM-HAADF) micrographs were recorded in order to investigate the crystal structure of the core–shell nanoparticles (Fig. 2d–e). Lattice fringes were observed across all the nanoparticles of each sample, attesting their high degree of crystallinity. Fast Fourier transforms (FFTs) were calculated from the representative nanoparticles (Fig. 2f–g). For all samples, the obtained spots correspond to interplanar distances that can be ascribed to the spinel structure. Due to the minor difference of the lattice parameters (see values below), $CoFe_2O_4$ and $NiFe_2O_4$ as well as mixed compositions cannot be distinguished from each other or from the $Fe_{3-\delta}O_4$ core. Looking closely to the HR-STEM micrographs in some regions of the shell of FeCoNi_10, and FeCoNi_14 (Fig. S3) nanoparticles, the lattice fringes close to the surface display half of the periodicity of lattice fringes of the core. It could be attributed to a minor presence of a wüstite phase which cell parameters (a_{CoO} = 4.2612 Å, JCPDS card n° 48-1719, a_{NiO} = 4.117 Å, JCPDS card n° 47-1049) are nearly half of those of the spinel phases.

The X-ray diffraction (XRD) (Fig. S4) patterns all show diffraction peaks which can be indexed to the spinel structure ($Fd\bar{3}m$ space group). Broad peaks were observed for each sample in agreement with nanometric sizes. The calculated Scherrer size is very close to the nanoparticle size measured from TEM micrographs for each sample (Table 1). Similar conclusions can be made from XRD patterns corresponding to FeCoNi_14 nanoparticles although peaks become narrower according to the larger size of pristine iron oxide nanoparticles. Unfortunately, due to peak broadening and similarity of cell parameters, the different ferrites (Fe_3O_4, $NiFe_2O_4$ and $CoFe_2O_4$) which are all spinel structures cannot be discriminated by XRD.[50] Refinement of XRD patterns allowed the calculation of cell parameters a for each nanoparticle (Table 1) showing a slight deviation from the theoretical value of Fe_3O_4 (a = 8.396 Å, JCPDS card n° 19-062), which we ascribe to the different chemical composition of the shell. A high content of $NiFe_2O_4$ (a = 8.339 Å, JCPDS card n° 10-0325) tends to decrease the cell parameter whereas a high content of $CoFe_2O_4$ (a = 8.392 Å, JCPDS card No. 00-022-1086) results in an unchanged value. Indeed, it is more appropriate to consider the crystal structure of core–shell nanoparticles as a continuous spinel phase with the Fe/Co atomic ratio evolving from the shell surface to the core center as we reported previously.[51] The calculated crystal sizes slightly differ from mean sizes measured from TEM micrographs which tend to be usually overestimated because the images results of 2D projections of nanoparticles which are not strictly spherical. Nevertheless, the similarities of these values for each sample testify to the single crystal structure of each nanoparticle whatever its chemical composition. It is worth noting that the XRD pattern of FeCoNi_10 displays unusual preferential orientation along (220) and (440) reflections. Although it could be ascribed to some anisotropic shape of nanoparticles as reported for cubic shape,[50,52] TEM micrographs did not reveal such a morphology.

The chemical composition of core–shell nanoparticles was investigated at high spatial resolution (down to 0.5 nm) using scanning transmission electron microscopy (STEM) coupled with electron energy loss spectroscopy spectrum imaging (EELS-SI) (Fig. 3). Therefore, the Fe, Co and Ni $L_{3,2}$ edges as well as the O K edge were acquired and quantified to obtain elemental maps. The overlap between the Ni $L_{3,2}$ edge and the Fe L_1 edge was corrected as we recently reported.[37] Iron exhibited the highest concentration in the core region, with its relative abundance decreasing toward the nanoparticle edges. In contrast, cobalt and nickel concentrations were found to generally increase toward the edges, indicating a shell enriched in these elements. This spatial distribution supports a core–shell architecture comprising a Fe_3O_4-rich core surrounded by a shell enriched in mixed metal ferrites ($Ni_{1-x}Co_xFe_2O_4$). Oxygen atoms were found to be homogeneously distributed throughout the nanoparticles with a slight increase in concentration towards the edges. This could be attributed to the preferential bonding of oxygen to cobalt and nickel atoms in the ferrite shell, or to the presence of adsorbed organic species, that were not fully removed during specimen cleaning.

A detailed analysis of the EELS results reveals some deviations from the ideal core–shell structure of the nanoparticles. The cobalt atoms are found to be non-homogeneously distributed throughout the shell of the FeCo nanoparticles (Fig. 3a), forming larger Co-rich domains and a variation of the local shell

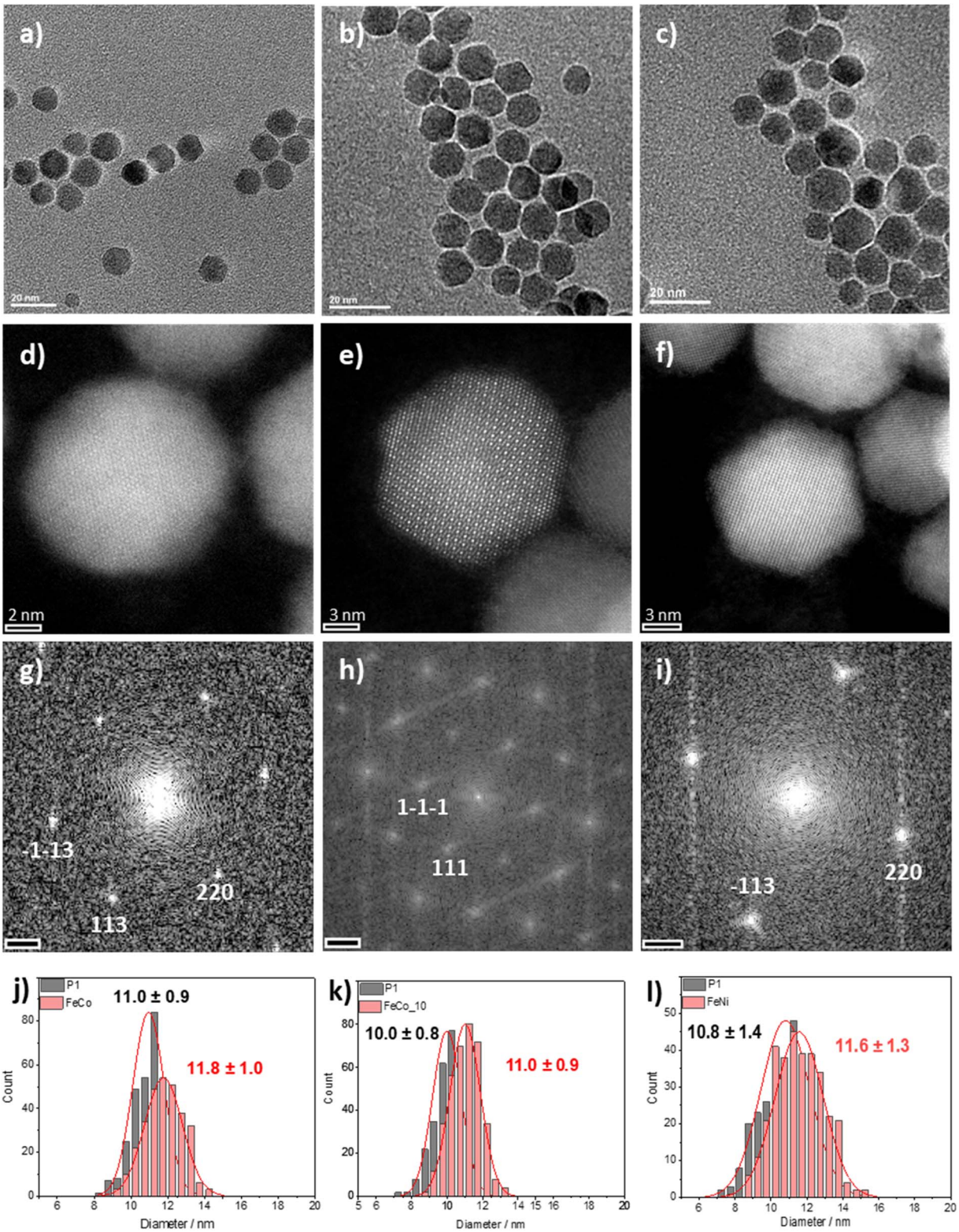

Fig. 2 TEM micrographs of (a) FeCo, (b) FeCoNi_10 and (c) FeNi nanoparticles and the corresponding (d–f) high-resolution STEM-HAADF micrographs. (g–i) FFT images calculated for the main nanoparticle of (d–f). (j–l) size distribution of pristine iron oxide and core–shell nanoparticles.

thickness. It could be explained by the preferential growth of CoO on specific facets of the nanoparticles and by a high concentration of Co monomers.[53] Nevertheless, the cobalt coverage seems to be complete, forming a continuous shell. In contrast, for FeNi nanoparticles, Fig. 3c suggests a non-homogeneous coverage of the Fe_3O_4 core by Ni atoms that

Table 1 Structural and chemical characteristics of core–shell nanoparticles

	FeCo	FeNi	FeCoNi_10	FeCoNi_14
Diameter (nm) – pristine (TEM)	11.0 ± 0.9	10.8 ± 1.3	10.0 ± 0.8	14.0 ± 1.1
Diameter (nm) – core–shell (TEM)	11.8 ± 1.0	11.6 ± 1.3	11.0 ± 0.9	14.8 ± 1.1
Apparent shell thickness (nm) (TEM)	0.4	0.4	0.5	0.4
Chemical composition of the shell (ICP-AES)	$Co_{1.38}Fe_{1.68}O_4$	$Ni_{0.9}Fe_{2.1}O_4$	$Ni_{0.8}Co_{0.42}Fe_{1.78}O_4$	$Ni_{0.67}Co_{0.63}Fe_{1.7}O_4$
Cell parameter (Å) (XRD)	8.39(3) ± 0.01	8.38(4) ± 0.01	8.38(6) ± 0.01	8.39(4) ± 0.01
Crystal size (nm) (XRD)	11.8 ± 0.1	11.2 ± 0.1	11.1 ± 0.1	14.3 ± 0.1

may be related to an insufficient concentration of Ni monomers. On the other hand, the shell of the FeCoNi_10 nanoparticles is highly homogeneous both in composition and thickness (Fig. 3b). According to STEM-EELS analysis, the chemical structures of the FeCo, FeNi and FeCoNi_10 nanoparticles agree with an iron oxide core with a $CoFe_2O_4$, $NiFe_2O_4$ and $Co_xNi_{1-x}Fe_2O_4$ shell grown at their surface, respectively. FeCoNi_14 nanoparticles also show a homogenous distribution of Co and Ni at their surface (Fig. S6) which is also ascribed to a $Co_xNi_{1-x}Fe_2O_4$ shell.

According to the periodicity of the lattice fringes seen by STEM-HAADF, a limited fraction of Co and Ni at the nanoparticle surface may be attributed to the formation of a wüstite phase ($Co_{1-x}Ni_xO$). The fact that this wüstite phase is located at the surface in such small fraction is in agreement with XRD patterns, which did not show any significant contribution of wüstite, thus representing less than 5% weight or corresponding to very small crystal sizes. It is also interesting to look in detail at the relative concentrations of Fe, Co, and Ni at the surface of the nanoparticles, *i.e.* the shell surface. For FeCo nanoparticles, the Co content was found to be higher (18–20 at%) than the stoichiometric value (14 at%) expected for $CoFe_2O_4$. For FeCoNi_10, the cumulated Co and Ni content (17–18 at%) is also higher than expected although Co and Ni content are relatively similar. In contrast, the Ni content at the surface of FeNi nanoparticles is slightly lower (10–13 at%) than expected for stoichiometric $NiFe_2O_4$. This reduced Ni content agrees with the observed incomplete coverage of the iron oxide core. All values differ from the expected stoichiometry of MFe_2O_4, showing for all samples (except FeNi), overloading of Co and/or Ni cations which confirms the relative concentration of Fe, Co and Ni measured by EELS at the shell surface. Similar conclusions can be made for FeCoNi_14 nanoparticles (Fig. S6). These compositional differences of the nanoparticle surface highlight the complexity of the formation mechanism of the shell in multicomponent ferrite nanoparticles.

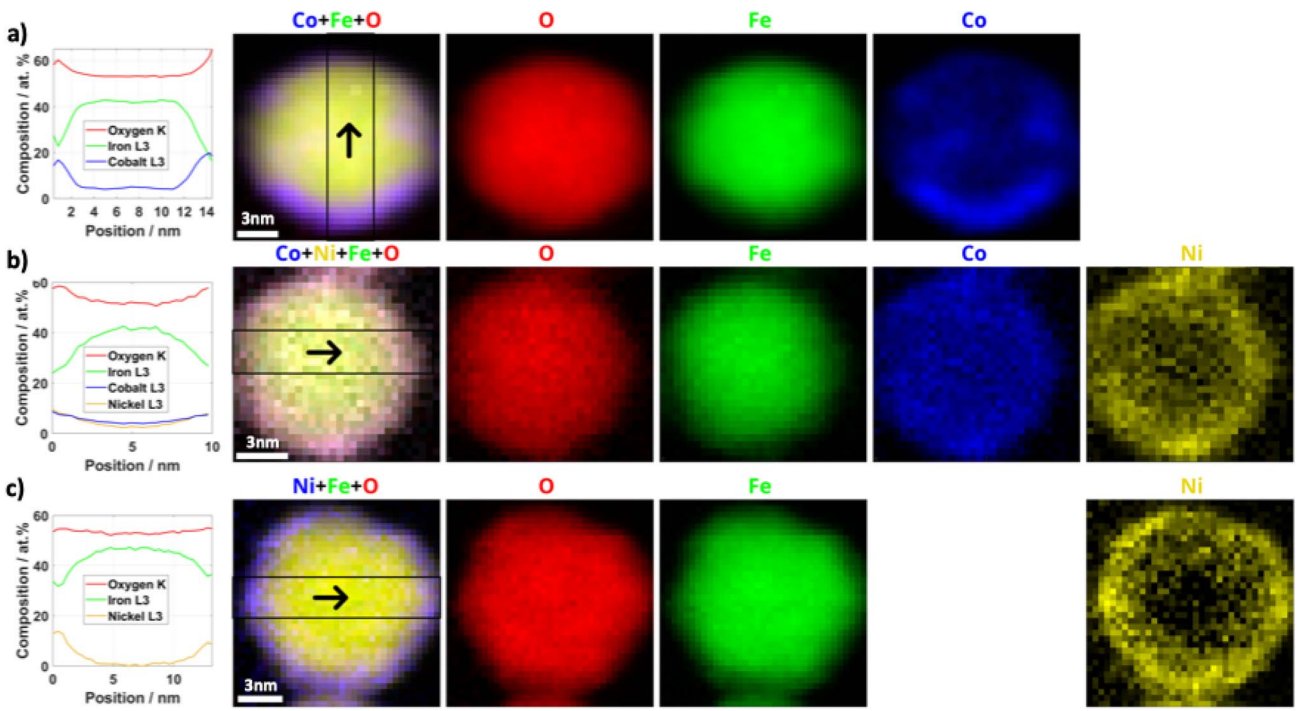

Fig. 3 STEM-EELS analysis of three individual nanoparticles of the three specimens (a) FeCo, (b) FeCoNi_10 and (c) FeNi. The first column shows profiles of the relative atomic percentages recorded across a single nanoparticle as indicated by an arrow in the chemical map shown in the second column. The following columns show the elemental maps of oxygen (red), iron (green), cobalt (blue) and nickel (yellow). Note that in the chemical map in (c), nickel is added in blue color to form a RGB composite map.

Soft X-ray absorption spectroscopy (XAS) and X-ray magnetic circular dichroism (XMCD) experiments were conducted to investigate the site occupancy and oxidation states of Fe and Co cations (Fig. 4). The isotropic XAS spectra acquired at the $L_{2,3}$ edges of Fe, Co, and Ni provide insight into the oxidation states and local coordination environments of the cations whether their spins are compensated or not. In particular, the Fe^{2+}/Fe^{3+} ratio in octahedral (O_h) sites can be qualitatively estimated from the intensity ratio of the I_1 and I_2 peaks (Fig. 4a).[54,55] The extracted values for core–shell nanoparticles are consistent with a distribution of Fe^{2+} and Fe^{3+} in a spinel structure. However, values exceeding that of pure Fe_3O_4 (0.71)[56]—as calculated for FeCo and FeCoNi_14—suggest an increased contribution from the wüstite phase (Fe_xO), consistent with recent findings in similar systems.[39] This likely arises from partial solubilization of the initial iron oxide nanoparticles during the second

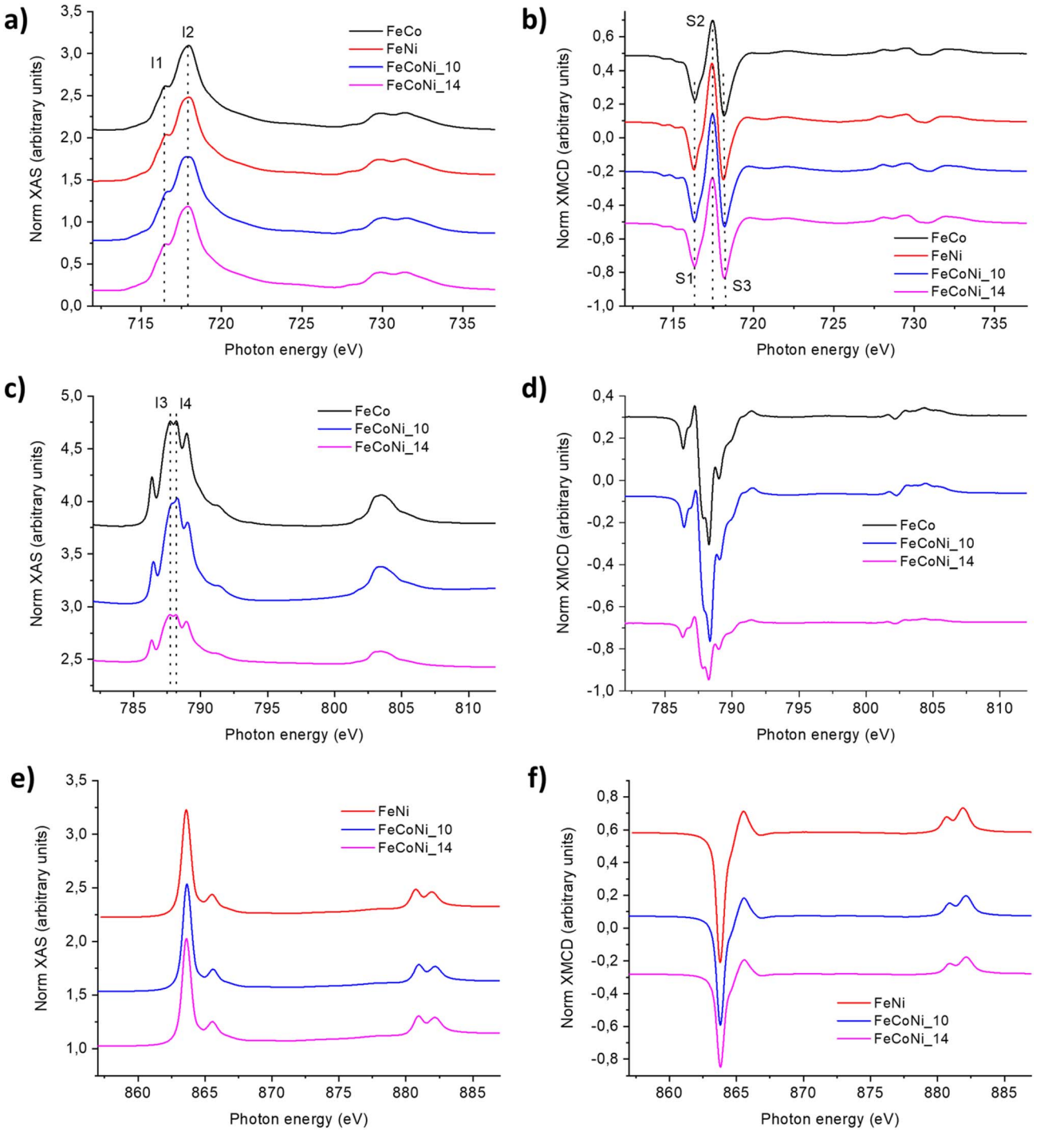

Fig. 4 (a,c and e) XAS and (b,d and f) XMCD spectra of FeCo, FeNi, FeCoNi_10 and FeCoNi_14 samples at the (a and b), the Fe $L_{2,3}$, (c and d) and the Co $L_{2,3}$, (e and f) at Ni $L_{2,3}$.

synthesis step, followed by recrystallization of Fe_xO within the shell. Such a process is plausibly driven by the stabilization of Fe(II) in the strongly reducing environment. Accordingly, the presence of Fe_xO in the shell is expected for all core–shell nanoparticles.

XMCD spectra provide complementary insights, as they are sensitive only to uncompensated magnetic moments (Fig. 4b). Thus, signals originate exclusively from ferrimagnetic phases—most notably spinel—while antiferromagnetic phases such as wüstite (with compensated spins) remain mostly XMCD-silent, except for spins at the nanoparticle surface which due to symmetry breaking may undergo a spin glass-like transition.[57] The XMCD spectra recorded at the Fe $L_{2,3}$ edges for all core–shell nanoparticles exhibit features characteristic of a reverse spinel structure. Peaks labeled S_1, S_2, and S_3 (Fig. 4b) correspond to Fe^{2+} and Fe^{3+} in O_h sites, Fe^{3+} in T_d sites, and Fe^{3+} in O_h sites, respectively. The intensity ratio $S=(S_1 + S_2)/(S_2 + S_3)$ provides an estimate of the relative content of Fe_3O_4 ($S = 1.14$)[48,58] *versus* γ-Fe_2O_3 ($S = 0.69$),[49,59] the latter being representative of MFe_2O_4 compositions. Based on this analysis, the Fe_3O_4 fraction in the core–shell nanoparticles are estimated to be 31%, 49%, 58%, and 42%, for FeCo, FeNi, FeCoNi_10 and FeCoNi_14, respectively (Table 2). Assuming that the shell grown at the surface of the pristine iron oxide nanoparticles and the reductive reaction medium avoid the oxidation of Fe^{2+}, we expect the counter fraction corresponds to the MFe_2O_4 shell.

XAS spectra recorded at the Co $L_{2,3}$ edges further clarify the distribution of Co^{2+} between spinel and wüstite phases (Fig. 4c). An I_4/I_3 intensity ratio greater than 1 [49,60] confirms the presence of CoO in FeCo, FeCoNi_10 and FeCoNi_14.[13,35] This finding, alongside the presence of FeO, suggests the formation of a mixed $Fe_xCo_{1-x}O$ wüstite phase in the shell, resulting from the co-crystallization of partially solubilized Fe species with Co added species as we previously observed for similar systems.[39] The corresponding XMCD spectra are characteristic of Co-ferrite, with a prominent negative peak attributed to uncompensated Co^{2+} spins occupying O_h sites in the spinel structure (Fig. 4d). Normalization of XMCD by the L_3 jump edge of XAS indicates that the estimated proportion of Co^{2+} with uncompensated spins is approximately 60%, 70% and 73% for FeCo, FeCoNi_10 and FeCoNi_14, respectively (Table 2). Nevertheless, we emphasize that this analysis remains qualitative. In particular, surface-related effects must be taken into account, as uncompensated magnetic moments at the surface can contribute to the XMCD signal. In any case, while the majority of Co^{2+} resides in the spinel lattice, a non-negligible fraction is incorporated into the wüstite phase.

XMCD spectra at the Ni $L_{2,3}$ edges for Ni-containing core–shell nanoparticles display a single negative peak, corresponding to Ni^{2+} occupying O_h sites in the spinel lattice (Fig. 4f). XAS spectra showing a single peak corresponding to Ni^{2+} (Fig. 4e), the normalization of XMCD by the L_3 jump edge of XAS indicates that a significant fraction of Ni^{2+}—21, 34 and 43% for FeNi, FeCoNi_10 and FeCoNi_14, respectively—is also incorporated into the wüstite phase.

Discussion on the formation mechanism and the chemical structure of nanoparticles

As we reported earlier,[13,35] the synthesis mechanism of core–shell nanoparticles in solution at high temperature (310 °C) involves the partial solubilization of the pristine iron oxide nanoparticle at their surface. Fe monomers subsequently co-crystallize with additional Co and/or Ni monomers resulting from the second thermal decomposition step in a spinel structure (MFe_2O_4). According to the respective thermal stability of Ni and Co complexes (see TG analysis for details, Fig. S8) as well as the relative reactivity of Fe, Co and Ni monomers, their growth kinetics are different. Therefore, as the formation of Co oxide (318 °C) takes place at a higher temperature than Ni oxide (293 °C), Co monomers are consumed at a slower rate than Ni ones upon the partial solubilization process of the iron oxide nanoparticles. It results in a different gradient of concentration from the iron oxide interface to the surface, Co being more concentrated at the resulting shell surface than Ni as shown by EELS-SI. Such a mechanism also explains the formation of Co-rich, thicker areas at the nanoparticle surface, where growth kinetics may be also favored by the higher concentration and reactivity of specific crystal planes that constitute the nanoparticle facets.[9,61]

According to the partial solubilization/co crystallization mechanism, we can assume that once Fe monomers are consumed by co-crystallization, any excess of Co or Ni monomers ultimately leads to the formation of a wüstite crystal structure ($Ni_xCo_{1-x}O$), at the surface of nanoparticles. If we consider that the partial solubilization kinetic is similar for all pristine nanoparticles, the kinetics of the formation of the shell through crystallization process is controlled by the concentration of metal complexes. Such an excess of Co and Ni as well as their atomic ratio at the shell surface is clearly supported by EELS-SI profiles.

Furthermore, the atomic ratio between the Co, Ni and $Co_{0.5}Ni_{0.5}$ complexes and the Fe complex used to form pristine iron oxide nanoparticles gives a good representation of the

Table 2 Intensity ratios of peaks calculated from XAS and XMCD spectra and the corresponding volume fractions

Sample	FeCo	FeNi	FeCoNi_10	FeCoNi_14	Fe_3O_4	γ-Fe_2O_3
I_1/I_2 ratio	0.87	0.65	0.65	0.89	0.71 [59]	0.35
S ratio	0.83	0.91	0.95	0.88	1.14 [47,59]	0.69 [48,59]
Fe_3O_4 (%)/MFe_2O_4 (%)	31/69	49/51	58/42	42/58	100/0	0/100
I_3/I_4 ratio	0.99	_	0.95	1.00		
$CoFe_2O_4$ (%)/CoO (%)	60/40	_	70/30	73/27		
$NiFe_2O_4$ (%)/NiO (%)	_	79/21	66/34	57/43		

relative concentration of M complexes. The M : Fe atomic ratio of FeCo, being higher (1 : 3) than that of FeNi (1 : 5), favors the formation of a larger fraction of CoO than NiO. For FeCoNi nanoparticles, a mixed $Co_{0.5}Ni_{0.5}St_2$ complex was used in order to favor the simultaneous formation of Co and Ni monomers (see TG analysis, Fig. S2), leading to the homogeneous distribution of both cations in the shell.

Magnetometry study

Zero field cooled (ZFC) and field cooled (FC) temperature-dependent magnetization curves were recorded successively upon cooling down from 400 K to 5 K in a 75 Oe magnetic field. As seen in the Fig. 5a. ZFC curves (hollow points) all show a maximum value that can be ascribed to the apparent blocking temperature (T_{MAX}), *i.e.*, the crossover temperature from a superparamagnetic state to a hysteretic one, taking into account dipolar interactions. Due to the size distribution of the nanoparticles, a distribution of apparent blocking temperatures exists and can be extracted as:[62]

$$f(T_{MAX}) = \mathrm{d}(M_{ZFC} - M_{FC})/\mathrm{d}T.$$

Such distribution for our nanoparticles can be found in Fig. 5b, and the position of its maximum, $\langle T_{MAX}\rangle$, is reported in Table 3. As the samples were measured in the powder state, strong dipolar interactions – which are known to increase T_{MAX}[61,62] may be expected. However, taking into account volume and magnetic moment variations across the samples, we can consider these to be roughly of the same order of magnitude (except for FeCoNi_14), within the series (see Fig. S20 and associated text, where the dipolar energies of the samples are estimated, assuming that the nanoparticles are separated by a distance equal to the length of two oleic acid molecules). Note that the former assumption does not neglect the effect of dipolar interaction on the relaxation of the macrospins, it only assumes this effect is similar in all the samples Thus, the evolution of $\langle T_{MAX}\rangle$ can be explained mainly in terms of the individual magnetic anisotropy of the nanoparticles and their volume (as $\langle T_{MAX}\rangle \approx \frac{K_{eff}V}{25k_B}$, K_{eff} being the effective anisotropy constant, V the volume of the nanoparticle and k_B the Boltzmann constant).

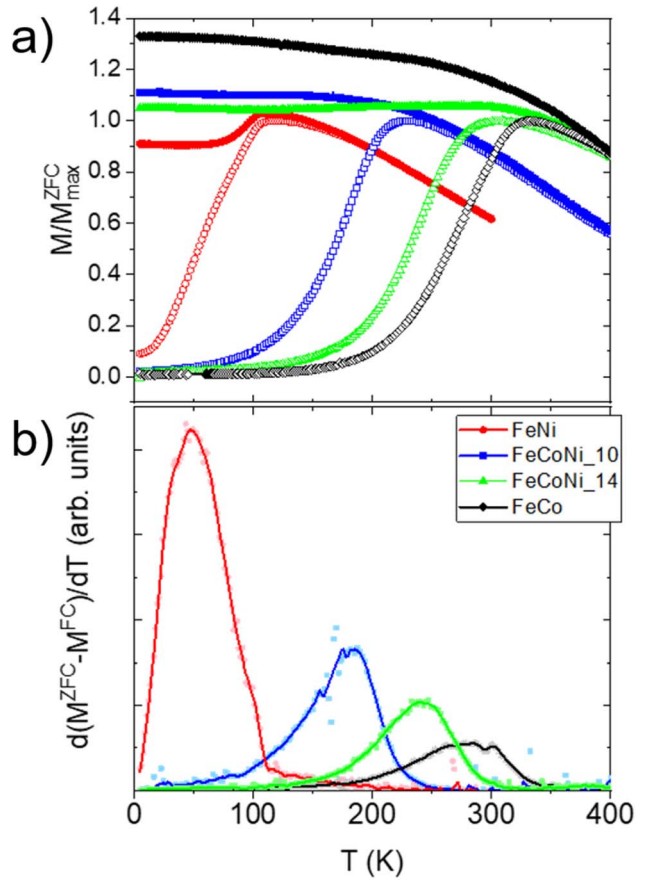

Fig. 5 (a) FC-ZFC magnetothermal curves recorded in a 75 Oe field and (b) its distribution of apparent blocking temperatures.

In this regard, Fig. 5a shows the samples with similar volume but with a different shell composition (FeCo, FeNi and FeCoNi_10) whose variation in T_{MAX} stems, in essence, from a change in the anisotropy energy of the core–shell nanoparticles. Indeed, the higher the Co/Ni ratio in these samples, the higher the T_{MAX} values, indicating that the Co-ferrite and mixed Co/Ni ferrite shells confer a higher anisotropy to the magnetite core by effective exchange interactions at the core–shell interface in FeCo and FeCoNi_10 respectively.[57] Interestingly, the addition of the nickel ferrite shell, lowers the overall anisotropy with respect to that of the core, in agreement with the anisotropy constant of $NiFe_2O_4$ ($K = 8 \times 10^3$ J m^3) (see Fig. S12 for the comparison of FeNi and the pristine core). Looking closely at the curves corresponding to FeNi, a flat shape of the FC and a drop in magnetization below T_{MAX} is observed, often attributed to a superspin glass freezing driven by strong dipolar interactions. This claim might seem at odds with the fact that dipolar interactions are of the same order of magnitude in all samples (Fig. S16). However, even if dipolar interactions are of the same order of magnitude, whether a collective freezing of the macrospins exists or not also depends on the magnetic anisotropy of the particles as reported by some of us.[63] Thus, it is consistent that the FeNi sample – exhibiting the lowest K_{eff}, see Tables 3 – is the only sample showing this marked feature.

Fig. 5a also depicts the FC-ZFC curves for FeCoNi samples, with different core sizes but similar shell composition (*i.e.*, mixed Ni/Co ferrite), where T_{MAX} (and also $\langle T_{MAX}\rangle$, see Fig. 5b) increases with the Co fraction (see Table 1 for the chemical composition). However, this may be accidental as the total particle volume is also increasing. Indeed, normalizing by the volume, the values of K_{eff} increase with the Ni/(Ni + Co) atomic ratio (see Table 3 for values), which is at odds with the expected effect of adding low anisotropy (Ni-containing) species. This anomaly can be attributed to the decreasing surface contribution to the global anisotropy with increasing volume, which seems to dominate the effects from the varying composition of the shell. Note that, even taking into account the magnitude of dipolar interactions in FeCoNi_14 with Ni/(Ni + Co) = 0.51

Table 3 Magnetic characteristics of nanoparticles

	FeCo	FeNi	FeCoNi_10	FeCoNi_14
Diameter (nm) – pristine	11.0 ± 0.9	10.8 ± 1.3	10.0 ± 0.8	14.0 ± 1.1
Diameter (nm) – core–shell	11.8 ± 1.0	11.6 ± 1.3	11.0 ± 0.9	14.8 ± 1.1
Chemical composition of the shell (ICP-AES)	$Co_{1.38}Fe_{1.68}O_4$	$Ni_{0.9}Fe_{2.1}O_4$	$Ni_{0.8}Co_{0.42}Fe_{1.78}O_4$	$Ni_{0.67}Co_{0.63}Fe_{1.7}O_4$
K_{eff} (kJ m^{-3})	112	23	91	48
T_{max} (K)	333	121	229	309
$\langle T_{MAX} \rangle$ (K)	279	43.5	184	235
M_S at 5 K	77.6	65.7	77.3	70.0
M_R/M_S at 5 K (ZFC)	0.71	0.34	0.56	0.6
H_C 5 K (ZFC) (Oe)	16600	327	4600	6800
H_C 5 K (FC) (Oe)	17600	279	4700	7200
H_E 5 K (Oe)	491	13	134	270

(Fig. S16), which will lower the actual K_{eff} of this sample, the qualitative trend will remain the same. In contrast, the samples with different shell compositions but similar volume (*i.e.*, FeCo, FeNi and FeCoNi_10) show the expected decrease of K_{eff} with Ni addition. Then, two different contributions are seen to dominate these magnetic anisotropy changes: (i) single-ion anisotropy in the series with similar core size and (ii) an increasingly high surface anisotropy contribution for the smaller nanoparticles in the FeCoNi series that shadows the effect of variations in the composition of the shell. It is interesting to note the consistency of the K_{eff} values (ranging from 20 to 110 kJ m^{-3}) with the one measured in a representative magnetite seed (K_{eff} = 51 kJ m^{-3}, obtained from the M(T) data (Fig. S12) as well as with those reported in literature for magnetite nanoparticles.[24,64]

To deepen our understanding on the effect of adding these hard/soft shells, we recorded hysteresis loops at 5 K (where the magnetic moments of nanoparticles are completely blocked in the timescale of the measurement) after cooling down in an applied field of 50 kOe (FC loops, Fig. 6a) as well as in zero field (ZFC loops, see Fig. S15 for comparison between them). In comparison to the corresponding pristine iron oxide nanoparticles P1 (Fig. S14), the associated coercive fields (H_C) of core–shell nanoparticles are much higher. As expected, FeCo nanoparticles exhibit the highest coercivity, while the progressive replacement of Co by Ni results in narrower loops. Such variation of the coercive field agrees with the intrinsic magnetic properties of the hard ($CoFe_2O_4$) and soft ($NiFe_2O_4$) magnetic materials. Note that, although FeCo hysteresis loops are, in fact, minor loops, the qualitative trend is not affected. In addition, FeCoNi nanoparticles display intermediate H_C values between those of FeCo and FeNi, even for larger core sizes, in agreement with their mixed chemical composition and their Co content. All hysteresis loops are smooth (no kinks are observed), indicating that hard and soft phases are completely exchange-coupled. According to STEM-EELS micrographs, Co and Ni are homogeneously distributed, thus resulting in a single hard phase which rotates coherently with the soft Fe_3O_4 magnetic core upon magnetic field reversal, thanks to a strong exchange coupling at their interface.[8]

However, values of the saturation magnetization (M_s) at 5 K (Table 3) show a non-monotonic behavior. Replacing Co with Ni in the octahedral sites (as confirmed by XMCD in Fig. 4f) decreases M_s from 77.6 to 58.9 emu/g from FeCo to FeNi, respectively, in agreement with the spin-only moment of Co^{2+} (3 μ_B) and Ni^{2+} (2 μ_B).[65] While FeCoNi_14 displays intermediate

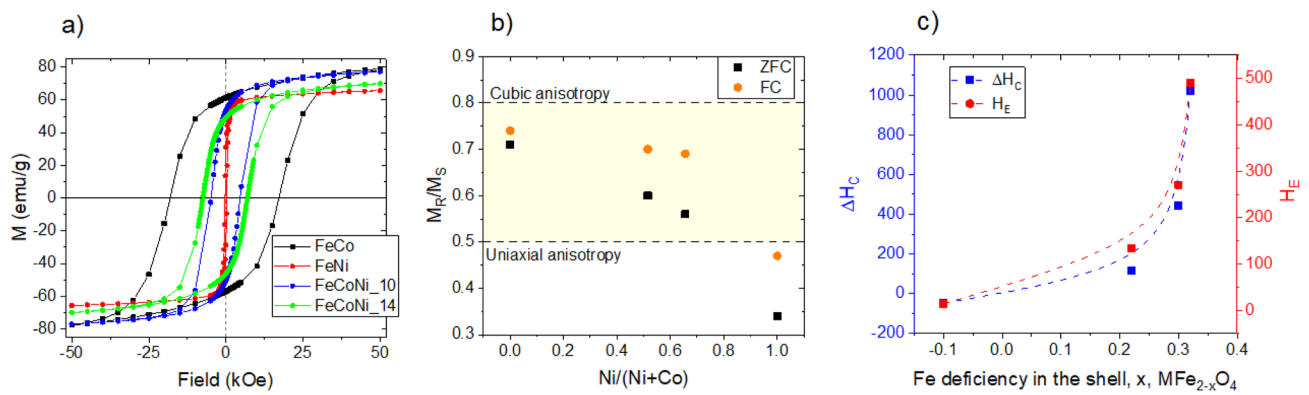

Fig. 6 (a) Hysteresis loops measured at 5 K after cooling in an applied field of 50 kOe. (b) Normalized values of the remanence magnetization (M_R/M_S) at 5 K calculated from M(H) curves recorded after cooling under an applied magnetic field of 5 T (FC) and after cooling with no applied field (ZFC). Values are plotted as a function of the Ni fraction, Ni/(Ni + Co). (c) Coercivity enhancement (ΔH_C) computed as the difference in coercivity of the FC and ZFC loop and exchange bias field (H_E) of the samples as a function of the deviation of Fe content in the shell from its stoichiometric value (*i.e.*, *x* in $MFe_{2-x}O_4$ where M is Ni and/or Co).

values, as expected, FeCoNi_10 shows a similar value as FeCo (*i.e.* 77 emu g^{-1}). Such high value, deviating from the overall trend, may be ascribed to less AFM content in the shell, whose existence has been proven by XMCD (see Fig. 4 and Table 2). Note that even if there is an overall trend in M_S values, this magnitude is strongly dependent of surface effect and exact AFM content that lowers their magnetization with respect to the bulk value of magnetite.[66] Reduced remanence magnetization (M_R/M_S) values, plotted in Fig. 6b for the ZFC and FC loops (and listed in Table 3) increase with Co content (or, alternatively, decrease with Ni fraction). Indeed, the addition of Co in the ferrite shell increases the M_R/M_S ratio from 0.34 (FeNi) to 0.54 (FeCoNi_10). Interestingly, FeCoNi_14 shows a ratio of 0.6 in accordance to its chemical composition. Yet, the magnitude of dipolar interactions in this sample may be affecting this value, the actual value being larger than this 0.6.[67] After the FC procedure, the loops get more squared due to unidirectional exchange coupling at the interface (larger coercivities and thus remanence). In fact, M_R/M_S values for the FeCoNi samples exhibit an almost constant value of 0.7 as depicted in Fig. 6c. All samples – except FeNi – show values of normalized remanence between the theoretical value for isolated monodomain nanoparticles with uniaxial anisotropy (0.5) and with cubic anisotropy (0.83–0.86).[68] This can be interpreted as a competition between uniaxial anisotropy and cubic anisotropy in the core–shell nanoparticles where the cubic contribution decreases with the addition of Ni, in line with the lower single-ion anisotropy of Ni^{2+} cations. Such intermediate values have been reported for other mixed Co and Ni ferrites.[14] However, for FeNi, the M_R/M_S value falls below 0.5 due to, dipolar interactions which are strong enough in comparison to effective anisotropy.[67] As observed in the FC-ZFC curve (Fig. 5a) and in the calculations of dipolar energy (Fig. S20), dipolar interactions in this sample were strong enough to render a superspin glass like-behavior.

FC curves recorded after cooling down to 5 K under an applied field of 5 T (Fig. 6a) are horizontally shifted to negative fields. This is indicative of unidirectional exchange coupling between, interfacial spins of the FiM soft core and those of the hard AFM shell.[69] The values of the associated exchange field (H_E) can be related to a different amount of AFM phase. The largest value of 491 Oe for the FeCo sample agree with the presence of CoO as we reported recently.[36] The anisotropy constant of CoO ($K_{CoO} = 5 \times 10^6$ J m^{-3}) being higher by two orders of magnitude than that of magnetite ($K_{Fe3O4} = 1 \times 10^4$ J m^{-3}), means that soft spins are pinned more strongly, thus requiring a higher magnetic field to reverse them. In contrast, FeNi exhibits a negligible exchange bias, which agrees with the low anisotropy of the NiO shell ($K_{NiO} = 8 \times 10^3$ J m^{-3}).[70] Additionally, FeCoNi_10 exhibits an intermediate value (134 Oe) according to the formation of a plausible $Co_xNi_{1-x}O$ AFM phase. Nevertheless, H_E values are rather low for all samples in comparison to core–shell nanoparticles with a thick CoO shell,[13,29,71,72] which agrees with small areas of wüstite observed at the nanoparticle surface in HR-STEM micrographs (see discussion above). As already mentioned, XMCD also shows the presence of a minority (yet non-negligible) of Ni^{2+} and Co^{2+} in the wüstite phase, in agreement with these low H_E values. Indeed, as it happened with M_S values, the magnitude of H_E (270 Oe for FeCoNi_14 and 134 Oe for FeCoNi_10) can be readily linked with the amount of AFM phase observed by XMCD (Table 2): the higher this amount, the higher the exchange bias field.

Furthermore, the elemental analysis concluded on non-stoichiometric shells with Fe deficiency (calculated as the deviation of the actual Fe content from the stoichiometric value, *i.e.*, x in $MFe_{2-x}O_4$ where M is Ni and/or Co). Remarkably, H_E shows a clear increasing trend with increasing Fe deficiency, corresponding to excess of Co and Ni, which in turn may be ascribed to the increasing presence of a $Co_xNi_{1-x}O$ AFM phase. This trend is depicted in Fig. 6c, along with the values of coercivity enhancement (ΔH_C), a phenomenon concomitant to exchange bias. Fig. 6c also includes the values of FeCo and FeNi, which correspond to the largest and the smallest H_E values, respectively. Both exchange bias and coercivity enhancement consistently follow the same qualitative trend, attesting that the Fe deficiency in the shell obtained by chemical analysis is directly related to the AFM content in the samples.

Finally, the relative Ni/(Ni + Co) atomic ratio in the shell may also be critical because of the significant difference of anisotropy between CoO and NiO, as observed for the FeCo and FeNi and samples. This trend is also seen in Fig. S17 where the exchange bias field decreases in an almost-linear fashion with this ratio. However, we cannot identify separately the Ni/Co atomic ratios in wüstite and spinel phases for each FeCoNi sample. All in all, the results indicate that the original core size of the nanoparticles does not have a clear effect on the strength of interfacial exchange coupling at 5 K, when all samples are well blocked, but it is a second order effect. The overall size, however, does affect the thermal stability of the samples as discussed above. Although interfacial exchange bias coupling is expected to have a minor contribution (yet far from negligible) on the increase of magnetic anisotropy in this study, it supports the information obtained by XMCD, *i.e.*, the presence of an additional wüstite phase to the spinel phase.

Conclusion

In this study, we investigated bimagnetic core–shell nanoparticles to elucidate how the chemical composition of the shell influences exchange coupling at the core–shell interface. The nanoparticles were synthesized *via* a two-step seed-mediated growth process, involving thermal decomposition of metal complexes in the presence of soft magnetic iron oxide seeds to promote the formation of a harder magnetic shell. A series of metal precursors (NiOct, CoSt, $Ni_{0.5}Co_{0.5}St_2$) were selected to decompose around 310 °C, aligning with the boiling point of octadecene used as the solvent. Shell formation occurred through a complex mechanism involving partial solubilization of the iron oxide surface, which released Fe monomers that subsequently co-crystallized with Ni and Co monomers. TEM revealed a consistent particle size increase (~1 nm in diameter), regardless of the metal precursor, indicating successful shell growth. Structural characterization by XRD and HRSTEM confirmed the formation of a defect-free spinel phase with coherent crystal continuity from the iron oxide core to the Co–

Ni ferrite shell, attributable to the minimal lattice mismatch between the two phases. XAS and XMCD analyses demonstrated that the majority of Co^{2+} and Ni^{2+} cations occupy octahedral sites within the spinel structure. EELS spectral imaging confirmed their homogeneous distribution across the shell, although FeCo nanoparticles exhibited localized thicker regions. ICP-MS elemental analysis further revealed that the Ni/Co ratio in the shell varies significantly depending on the amount of metal precursor used, highlighting the influence of precursor decomposition kinetics on the co-crystallization process.

In addition to the spinel structure, HRSTEM occasionally revealed lattice fringe periodicities consistent with a secondary wüstite phase ($Ni_{1-x}Co_xO$), primarily at the nanoparticle edges. This assignment was supported by EELS mapping and corroborated by XAS and XMCD spectra, which indicated a minor yet discernible fraction of magnetically compensated Ni and Co spins characteristic of an antiferromagnetic (AFM) wüstite phase. The formation of this phase is attributed to the depletion of free Fe monomers during co-crystallization. Various amounts of the wüstite phase were observed, depending on the sample which may be ascribed to different kinetics of the reaction. Unfortunately, it was not possible to calculate the Co/Ni atomic ratio separately for the spinel and the wüstite phases.

The magnetic properties of the core–shell nanoparticles were governed predominantly by the shell's chemical composition. For a given core size, a higher Co/Ni ratio led to increased blocking temperatures, in agreement with the higher magnetic anisotropy of $CoFe_2O_4$ relative to $NiFe_2O_4$. However, despite this trend, the overall effective magnetic anisotropy decreased with increasing core size and Co content, indicating that surface anisotropy—enhanced by nanoparticle size reduction—plays a dominant role. The AFM wüstite phase ($Ni_{1-x}Co_xO$) contributed to the overall magnetic behavior through unidirectional exchange coupling with the spinel shell, particularly enhancing effective anisotropy in Co-rich systems due to the intrinsically higher anisotropy of CoO compared to NiO. Nevertheless, this contribution was modest, as evidenced by the relatively low exchange bias field values.

This work highlights the complex growth mechanisms underlying bimagnetic core–shell nanoparticle synthesis *via* thermal decomposition and demonstrates how the chemical nature of the metal precursors governs shell composition, structural integrity, and magnetic performance. These findings provide valuable insights for tailoring the nanoscale magnetic architecture and interfacial exchange interactions in core–shell systems for advanced magnetic applications.

Conflicts of interest

The authors declare no conflicts of interest in this study.

Data availability

Data for this article, including TEM micrographs, EELS mapping, XRD patterns and magnetic data are available at Seafile Unistra at https://seafile.unistra.fr/d/d68569bc9fe64f289787/. The data supporting this article have been included as part of the supplementary information (SI). Supplementary information: infrared spectra and thermal gravimetric analysis of the metal precursors. TEM micrographs of pristine iron oxide nanoparticles. Size distribution, HRTEM, electronic diffraction patterns, and EELS SI analysis of FeCoNi_14 nanoparticles. Infrared spectra, XRD patterns, TG analysis, compared XAS and XMCD spectra and additional magnetic data of all nanoparticles. See DOI: https://doi.org/10.1039/d6na00118a.

Acknowledgements

B.P. and I.M. acknowledge support from IdEx University of Strasbourg. J.A.D.T. and R.L.-M. acknowledge support from Junta de Comunidades de Castilla-La Mancha [SPBLY/21/180501/000226] and Ministerio de Ciencia, Innovación y Universidades [PID2022142267NB-I00]. B.P., I.M. and F.D. acknowledge the SOLEIL synchrotron for beamtime allocation at the DEIMOS beamline. R.A. and S.H. acknowledge funding from the Spanish MICIU (PID2023-151080NB-I00/AEI/10.13039/501100011033) and CEX2023-001286-S MICIU/AEI/10.13039/501100011033) as well from the Gobierno de Aragón (DGA) under project E13-23R. STEM imaging and spectroscopic (EELS) studies have been conducted in the Laboratorio de Microscopias Avanzadas (LMA) at Universidad de Zaragoza.

References

1 J. Gao, H. Gu and B. Xu, *Acc. Chem. Res.*, 2009, **42**, 1097–1107.
2 S. Bedanta and W. Kleemann, *J. Phys. Appl. Phys.*, 2008, **42**, 013001.
3 O. Gutfleisch, M. A. Willard, E. Brück, C. H. Chen, S. G. Sankar and J. P. Liu, *Adv. Mater.*, 2011, **23**, 821–842.
4 A. López-Ortega, M. Estrader, G. Salazar-Alvarez, A. G. Roca and J. Nogués, *Phys. Rep.*, 2015, **553**, 1–32.
5 S. Massari and M. Ruberti, *Resour. Policy*, 2013, **38**, 36–43.
6 E. Lottini, A. López-Ortega, G. Bertoni, S. Turner, M. Meledina, G. Van Tendeloo, C. de Julián Fernández and C. Sangregorio, *Chem. Mater.*, 2016, **28**, 4214–4222.
7 J.-H. Lee, J. Jang, J. Choi, S. H. Moon, S. Noh, J. Kim, J.-G. Kim, I.-S. Kim, K. I. Park and J. Cheon, *Nat. Nanotechnol.*, 2011, **6**, 418–422.
8 Q. Song and Z. J. Zhang, *J. Am. Chem. Soc.*, 2012, **134**, 10182–10190.
9 X. Liu, B. P. Pichon, C. Ulhaq, C. Lefèvre, J.-M. Grenèche, D. Bégin and S. Bégin-Colin, *Chem. Mater.*, 2015, **27**, 4073–4081.
10 A. López-Ortega, E. Lottini, G. Bertoni, C. de Julián Fernández and C. Sangregorio, *Chem. Mater.*, 2017, **29**, 1279–1289.
11 N. Daffé, M. Sikora, M. Rovezzi, N. Bouldi, V. Gavrilov, S. Neveu, F. Choueikani, P. Ohresser, V. Dupuis, D. Taverna, A. Gloter, M.-A. Arrio, P. Sainctavit and A. Juhin, *Adv. Mater. Interfaces*, 2017, **4**, 1700599.
12 S. D. Oberdick, A. Abdelgawad, C. Moya, S. Mesbahi-Vasey, D. Kepaptsoglou, V. K. Lazarov, R. F. L. Evans, D. Meilak,

E. Skoropata, J. van Lierop, I. Hunt-Isaak, H. Pan, Y. Ijiri, K. L. Krycka, J. A. Borchers and S. A. Majetich, *Sci. Rep.*, 2018, **8**, 3425–3437.
13 K. Sartori, G. Cotin, C. Bouillet, V. Halte, S. Begin-Colin, F. Choueikani and B. P. Pichon, *Nanoscale*, 2019, **11**, 12946–12958.
14 A. Omelyanchik, S. Villa, F. Locardi, A. M. Ferretti, A. Ponti, G. Singh, G. Barucca, S. Slimani, A. Del Tedesco, P. Riello, B. Rutkowski, M. Vasilakaki, G. Margaris, K. N. Trohidou and D. Peddis, *Chem. Mater.*, 2024, **36**, 7976–7987.
15 A. Broese van Groenou, P. F. Bongers and A. L. Stuyts, *Mater. Sci. Eng.*, 1969, **3**, 317–392.
16 D. Carta, M. F. Casula, A. Falqui, D. Loche, G. Mountjoy, C. Sangregorio and A. Corrias, *J. Phys. Chem. C*, 2009, **113**, 8606–8615.
17 J. F. Hochepied, P. Sainctavit and M. P. Pileni, *J. Magn. Magn. Mater.*, 2001, **231**, 315–322.
18 M. Albino, E. Fantechi, C. Innocenti, A. López-Ortega, V. Bonanni, G. Campo, F. Pineider, M. Gurioli, P. Arosio, T. Orlando, G. Bertoni, C. de Julián Fernández, A. Lascialfari and C. Sangregorio, *J. Phys. Chem. C*, 2019, **123**, 6148–6157.
19 P. Coppola, F. G. da Silva, G. Gomide, F. L. O. Paula, A. F. C. Campos, R. Perzynski, C. Kern, J. Depeyrot and R. Aquino, *J. Nanoparticle Res.*, 2016, **18**, 1–15.
20 J. M. D. Coey, *Magnetism and Magnetic Materials*, Cambridge Univ. Press, Cambridge, Repr, 2013.
21 T. P. Almeida, F. Moro, M. W. Fay, Y. Zhu and P. D. Brown, *J. Nanoparticle Res.*, 2014, **16**, 2395.
22 A. Omelyanchik, S. Villa, M. Vasilakaki, G. Singh, A. M. Ferretti, A. Ponti, F. Canepa, G. Margaris, K. N. Trohidou and D. Peddis, *Nanoscale Adv.*, 2021, **3**, 6912–6924.
23 J. Park, K. An, Y. Hwang, J.-G. Park, H.-J. Noh, J.-Y. Kim, J.-H. Park, N.-M. Hwang and T. Hyeon, *Nat. Mater.*, 2004, **3**, 891–895.
24 A. Demortiere, P. Panissod, B. P. Pichon, G. Pourroy, D. Guillon, B. Donnio and S. Begin-Colin, *Nanoscale*, 2011, **3**, 225–232.
25 W. Baaziz, B. P. Pichon, S. Fleutot, Y. Liu, C. Lefevre, J.-M. Greneche, M. Toumi, T. Mhiri and S. Begin-Colin, *J. Phys. Chem. C*, 2014, **118**, 3795–3810.
26 S. Sun, H. Zeng, D. B. Robinson, S. Raoux, P. M. Rice, S. X. Wang and G. Li, *J. Am. Chem. Soc.*, 2004, **126**, 273–279.
27 M. Estrader, A. López-Ortega, S. Estradé, I. V. Golosovsky, G. Salazar-Alvarez, M. Vasilakaki, K. N. Trohidou, M. Varela, D. C. Stanley, M. Sinko, M. J. Pechan, D. J. Keavney, F. Peiró, S. Suriñach, M. D. Baró and J. Nogués, *Nat. Commun.*, 2013, **4**, 2960.
28 G. C. Lavorato, E. Lima, H. E. Troiani, R. D. Zysler and E. L. Winkler, *Nanoscale*, 2017, **9**, 10240–10247.
29 I. Panagiotopoulos, G. Basina, V. Alexandrakis, E. Devlin, G. Hadjipanayis, L. Colak, D. Niarchos and V. Tzitzios, *J. Phys. Chem. C*, 2009, **113**, 14609.
30 A. Omelianchik, G. Singh, B. H. McDonagh, V. Rodionova, D. Fiorani, D. Peddis and S. Laureti, *Nanotechnology*, 2018, **29**, 055703.
31 G. Salazar-Alvarez, H. Lidbaum, A. López-Ortega, M. Estrader, K. Leifer, J. Sort, S. Suriñach, M. D. Baró and J. Nogués, *J. Am. Chem. Soc.*, 2011, **133**, 16738–16741.
32 K. L. Krycka, J. A. Borchers, M. Laver, G. Salazar-Alvarez, A. Lopez-Ortega, M. Estrader, S. Surinach, M. D. Baro, J. Sort and J. Nogués, *J. Appl. Phys.*, 2013, **113**, 17B531.
33 V. Gavrilov-Isaac, S. Neveu, V. Dupuis, D. Taverna, A. Gloter and V. Cabuil, *Small*, 2015, **11**, 2614–2618.
34 K. Sartori, F. Choueikani, A. Gloter, S. Begin-Colin, D. Taverna and B. P. Pichon, *J. Am. Chem. Soc.*, 2019, **141**, 9783–9787.
35 K. Sartori, A. Musat, F. Choueikani, J.-M. Grenèche, S. Hettler, P. Bencok, S. Begin-Colin, P. Steadman, R. Arenal and B. P. Pichon, *ACS Appl. Mater. Interfaces*, 2021, **13**, 16784–16800.
36 K. Sartori, R. Lopez-Martin, F. Choueikani, A. Gloter, J.-M. Grenèche, S. Begin-Colin, D. Taverna, J. A. D. Toro and B. P. Pichon, *Nanoscale Adv.*, 2024, **6**, 2903–2918.
37 S. Hettler and R. Arenal, *Micron*, 2025, **196–197**, 103858.
38 P. Ohresser, E. Otero, F. Choueikani, K. Chen, S. Stanescu, F. Deschamps, T. Moreno, F. Polack, B. Lagarde, J.-P. Daguerre, F. Marteau, F. Scheurer, L. Joly, J.-P. Kappler, B. Muller, O. Bunau and Ph. Sainctavit, *Rev. Sci. Instrum.*, 2014, **85**, 013106.
39 K. Sartori, D. Ihiawakrim, C. Lefèvre, S. Reguer, C. Mocuta, S. Bégin-Colin, F. Choueikani and B. P. Pichon, *Mater. Adv.*, 2022, **3**, 8716–8728.
40 G. Salazar-Alvarez, J. Sort, A. Uheida, M. Muhammed, S. Surinach, M. D. Baro and J. Nogues, *J. Mater. Chem.*, 2007, **17**, 322.
41 A. Juhin, A. López-Ortega, M. Sikora, C. Carvallo, M. Estrader, S. Estradé, F. Peiró, M. Dolors Baró, P. Sainctavit, P. Glatzel and J. Nogués, *Nanoscale*, 2014, **6**, 11911–11920.
42 S. Lentijo-Mozo, D. Deiana, E. Sogne, A. Casu and A. Falqui, *Chem. Mater.*, 2018, **30**, 8099–8112.
43 K. Sartori, A. Musat, F. Choueikani, J.-M. Grenèche, S. Hettler, P. Bencok, S. Begin-Colin, P. Steadman, R. Arenal and B. P. Pichon, *ACS Appl. Mater. Interfaces*, 2021, **13**, 16784–16800.
44 G. Cotin, C. Kiefer, F. Perton, M. Boero, B. Özdamar, A. Bouzid, G. Ori, C. Massobrio, D. Begin, B. Pichon, D. Mertz and S. Begin-Colin, *ACS Appl. Nano Mater.*, 2018, **1**, 4306–4316.
45 F. Perton, G. Cotin, C. Kiefer, J.-M. Strub, S. Cianferani, J.-M. Greneche, N. Parizel, B. Heinrich, B. Pichon, D. Mertz and S. Begin-Colin, *Inorg. Chem.*, 2021, **60**, 12445–12456.
46 R. F. Egerton, *Electron Energy-Loss Spectroscopy in the Electron Microscope*, Springer US, Boston, MA, 2011.
47 P. Ohresser, E. Otero, F. Choueikani, K. Chen, S. Stanescu, F. Deschamps, T. Moreno, F. Polack, B. Lagarde and J.-P. Daguerre, *Rev. Sci. Instrum.*, 2014, **85**, 013106.
48 N. Daffé, F. Choueikani, S. Neveu, M.-A. Arrio, A. Juhin, P. Ohresser, V. Dupuis and P. Sainctavit, *J. Magn. Magn. Mater.*, 2018, **460**, 243–252.
49 K. Sartori, A. Musat, F. Choueikani, J.-M. Grenèche, S. Hettler, P. Bencok, S. Begin-Colin, P. Steadman,

R. Arenal and B. P. Pichon, *ACS Appl. Mater. Interfaces*, 2021, **13**, 16784–16800.
50 L. Song, C. Yan, W. Zhang, H. Wu, Z. Jia, M. Ma, J. Xie, N. Gu and Y. Zhang, *J. Nanomater.*, 2016, **2016**, 1–8.
51 K. Sartori, D. Ihiawakrim, C. Lefèvre, S. Reguer, C. Mocuta, S. Bégin-Colin, F. Choueikani and B. P. Pichon, *Mater. Adv.*, 2022, **3**, 8716–8728.
52 H. Yang, T. Ogawa, D. Hasegawa and M. Takahashi, *J. Appl. Phys.*, 2008, **103**, 07D526.
53 I. Makarchuk, B. Rotonnelli, L. Royer, S. Hettler, J.-J. Gallet, F. Bournel, J. Guehl, A. Brige, A. Zitolo, G. Kéranguéven, A. Bonnefont, R. Arenal, E. Savinova, T. Asset and B. P. Pichon, *Chem. Mater.*, 2025, **37**, 833–844.
54 E. Pellegrin, M. Hagelstein, S. Doyle, H. O. Moser, J. Fuchs, D. Vollath, S. Schuppler, M. A. James, S. S. Saxena, L. Niesen, O. Rogojanu, G. A. Sawatzky, C. Ferrero, M. Borowski, O. Tjernberg and N. B. Brookes, *Phys. Status Solidi B*, 1999, **215**, 797–801.
55 J. Li, N. Menguy, M.-A. Arrio, P. Sainctavit, A. Juhin, Y. Wang, H. Chen, O. Bunau, E. Otero, P. Ohresser and Y. Pan, *J. R. Soc., Interface*, 2016, **13**, 20160355.
56 E. Pellegrin, M. Hagelstein, S. Doyle, H. O. Moser, J. Fuchs, D. Vollath, S. Schuppler, M. A. James, S. S. Saxena, L. Niesen, O. Rogojanu, G. A. Sawatzky, C. Ferrero, M. Borowski, O. Tjernberg and N. B. Brookes, *Phys. Status Solidi B*, 1999, **215**, 797–801.
57 A. G. Roca, I. V. Golosovsky, E. Winkler, A. López-Ortega, M. Estrader, R. D. Zysler, M. D. Baró and J. Nogués, *Small*, 2018, **14**, 1703963.
58 A. Feld, A. Weimer, A. Kornowski, N. Winckelmans, J.-P. Merkl, H. Kloust, R. Zierold, C. Schmidtke, T. Schotten, M. Riedner, S. Bals and H. Weller, *ACS Nano*, 2019, **13**, 152–162.
59 P. Jungcharoen, M. Pédrot, F. Choueikani, M. Pasturel, K. Hanna, F. Heberling, M. Tesfa and R. Marsac, *Environ. Sci.:Nano*, 2021, **8**, 2098–2107.
60 I. J. Bruvera, P. Mendoza Zélis, M. Pilar Calatayud, G. F. Goya and F. H. Sánchez, *J. Appl. Phys.*, 2015, **118**, 184304.
61 M. Pauly, B. P. Pichon, P.-A. Albouy, S. Fleutot, C. Leuvrey, M. Trassin, J.-L. Gallani and S. Begin-Colin, *J. Mater. Chem.*, 2011, **21**, 16018–16027.
62 J. A. De Toro, P. S. Normile, S. S. Lee, D. Salazar, J. L. Cheong, P. Muñiz, J. M. Riveiro, M. Hillenkamp, F. Tournus, A. Tamion and P. Nordblad, *J. Phys. Chem. C*, 2013, **117**, 10213–10219.
63 E. H. Sánchez, M. Vasilakaki, S. S. Lee, P. S. Normile, M. S. Andersson, R. Mathieu, A. López-Ortega, B. P. Pichon, D. Peddis, C. Binns, P. Nordblad, K. Trohidou, J. Nogués and J. A. De Toro, *Small*, 2022, **18**, 2106762.
64 P. García-Acevedo, M. A. González-Gómez, Á. Arnosa-Prieto, L. de Castro-Alves, Y. Piñeiro and J. Rivas, *Adv. Sci.*, 2023, **10**, 2203397.
65 M. Baričić, P. Maltoni, G. Barucca, N. Yaacoub, A. Omelyanchik, F. Canepa, R. Mathieu and D. Peddis, *Phys. Chem. Chem. Phys.*, 2024, **26**, 6325–6334.
66 Y. Hadadian, H. Masoomi, A. Dinari, C. Ryu, S. Hwang, S. Kim, B. ki Cho, J. Y. Lee and J. Yoon, *ACS Omega*, 2022, **7**, 15996–16012.
67 B. Geng, Z. Ding and Y. Ma, *Nano Res.*, 2016, **9**, 2772–2781.
68 N. A. Usov and S. E. Peschany, *J. Magn. Magn. Mater.*, 1997, **174**, 247–260.
69 J. Nogues, J. Sort, V. Langlais, V. Skumryev, S. Surinach, J. S. Munoz and M. D. Baro, *Phys. Rep.*, 2005, **422**, 65–117.
70 M. Tadic, D. Nikolic, M. Panjan and G. R. Blake, *J. Alloys Compd.*, 2015, **647**, 1061–1068.
71 X. Liu, B. P. Pichon, C. Ulhaq, C. Lefèvre, J.-M. Grenèche, D. Bégin and S. Bégin-Colin, *Chem. Mater.*, 2015, **27**, 4073–4081.
72 E. Skoropata, R. D. Desautels, C.-C. Chi, H. Ouyang, J. W. Freeland and J. van Lierop, *Phys. Rev. B*, 2014, **89**, 024410.

